JBIC Journal of Biological Inorganic Chemistry
https://doi.org/10.1007/s00775-021-01873-9

ORIGINAL PAPER

Synthesis, structure and anticancer properties of new biotin- and morpholine-functionalized ruthenium and osmium half-sandwich complexes

Mickaël Marloye[1] · Haider Inam[2] · Connor J. Moore[2] · Vinciane Debaille[3] · Justin R. Pritchard[2] · Michel Gelbcke[1] · Franck Meyer[1] · François Dufrasne[1] · Gilles Berger[1,4]

Received: 5 May 2021 / Accepted: 15 June 2021

Abstract

Ruthenium (Ru) and osmium (Os) complexes are of sustained interest in cancer research and may be alternative to platinum-based therapy. We detail here three new series of ruthenium and osmium complexes, supported by physico-chemical characterizations, including time-dependent density functional theory, a combined experimental and computational study on the aquation reactions and the nature of the metal–arene bond. Cytotoxic profiles were then evaluated on several cancer cell lines although with limited success. Further investigations were, however, performed on the most active series using a genetic approach based on RNA interference and highlighted a potential multi-target mechanism of action through topoisomerase II, mitotic spindle, HDAC and DNMT inhibition.

Graphic abstract

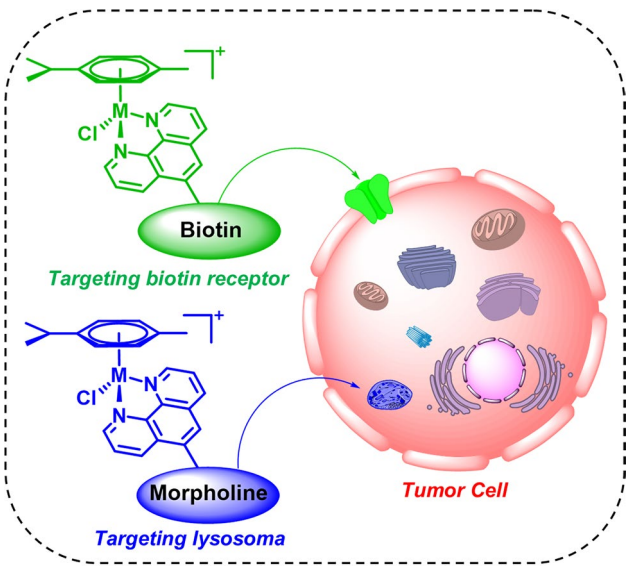

Keywords Metallodrug · shRNA profiling · Anticancer complex · Cell targeting · Metal–arene

✉ Gilles Berger
gilles.berger@ulb.be

Extended author information available on the last page of the article

Published online: 26 June 2021

Introduction

Metal complexes have been a part of the anticancer arsenal since the early 60s and the discovery of cisplatin by Rosenberg, Van Camp and Krigas [1]. Despite the utmost importance of platinum (Pt) therapy in cancer treatment, severe side effects and resistance turned attention to neighboring metals [2, 3]. Ru complexes emerged as potential candidates but if three of them entered trials [4], a non-platinum drug has yet to be approved in the clinics. NAMI-A failed to show sufficient phase II efficacy in combination with gemcitabine for non-small cell lung cancer [4, 5], KP1019 showed good efficacy in phase I but was soon substituted by its sodium salt analogue NKP-1339 for further investigations and to date, NKP-1339 only completed a phase I escalation study to treat advanced solid tumors [4]. The second-generation Ru complexes belong to the pseudo-octahedral family (also called half-sandwich or piano-stool) and comprise promising preclinical compounds, such as RM175 that showed in vitro and in vivo efficiency on primary tumors and cisplatin-resistant cell lines [6]. Another half-sandwich series, the so-called RAPTA family, has limited in vitro activity but good in vivo anti-metastatic properties [7, 8]. Sharing similar electronic configurations to their Ru counterparts, low-spin d^6 Os complexes naturally followed, although being more kinetically inert [9, 10]. Recently, an Os^{II} arene complex [Os(η^6-*p*-cym)(azpy-NMe_2)I]PF_6, namely FY26 (where azpy is for azopyridine) has received attention for its ability to generate reactive oxygen species (ROS) after hydrolytic activation mediated by glutathione (GSH) [11]. Precise intracellular targets remained elusive but proteomic have allowed significant progress. It has been proposed that NKP1339 interacts with ribosomal proteins, resulting in endoplasmic reticulum perturbation and downregulation of the heat shock protein GRP78, which plays an important role in the unfolded protein response (UPR) [12–14]. It is also worth mentioning the Ru^{II} arene complexes bearing pyridinecarbothioamide ligands that target a specific protein scaffold, pectin, i.e. plectin, which is a cytolinker protein associated to non-mitotic microtubules [15].

We here made an attempt to target cancer cells and lysosomes by specific groups on the metal or ligand. Lysosome-targeting was attempted by functionalization of Ru^{II} and Os^{II} half-sandwich complexes with a morpholino group [16]. Weak bases such as morpholine are partly neutral in the cytoplasm and can diffuse into the lysosomes, where they get trapped by the more acidic lysosomal pH [17]. Metal arene complexes can also react with soft bionucleophiles, especially S-donors like thiol side chains of proteins, or GSH [11, 18]. Therefore, interactions of these compounds with lysosomal thiol-containing proteins, such as the L and B cysteine cathepsins that are associated with tumor invasion and metastasis [19], could disturb lysosomal function, sensitizing them to apoptosis [20]. The relationship between cathepsin B inhibition and the anticancer activity of Ru^{II} RAPTA compounds was highlighted by in vitro assays and confirmed by molecular docking [21]. Ru^{II} *p*-cymene complexes bearing 1,3-indandione ligand and fine-tuned with *N*-donor morpholine leaving groups demonstrated low micromolar activity against human colon adenocarcinoma cell line SW480 [22]. Photoactive Ru^{II} complexes functionalized with a morpholine moiety were recently reported as theranostic agents targeting lysosomes [23].

The more general approach that we took consisted in linking biotin as the targeting group. Biotin receptors are known to be overexpressed by various cancer cells lines [24], and such conjugates also have demonstrated their potential for tumor targeting. Among them, several biotinyl Pt [25, 26] and Ru [27] complexes have been disclosed. Recently, Valente et al. reported new $Ru^{II}(\eta^5\text{-}C_5H_5)$ biotin-based complexes with low IC_{50} values on the invasive MDA-MB-231 breast cell line due to increased cellular uptake mediated by the main biotin receptor, the sodium-dependent multivitamin transporter (SMVT) [28]. These compounds were further reported to be up to 1390-fold more potent than cisplatin on cisplatin-resistant cells, due to their ability to inhibit the multidrug resistance-associated protein 1 (MRP1) and the P-glycoprotein 1 (Pgp) transporters [29].

We, therefore, report here the synthesis, physico-chemical characterization and preliminary biological data of six new Ru^{II} and Os^{II} organometallic complexes. After a structural analysis both in the solid state and in solution, we highlight divergent reactivities with water by ^{1}H NMR and mass spectrometry (MS) for complexes bearing a 1,10-phenanthroline ligand and their analogues with 4-(2-aminoethyl)morpholine. We thus made use of computational tools to delineate these features and further looked at the nature of the metal–arene bond by explicitly calculating the amount of donor–acceptor interactions between orbitals. This series of new complexes did not prove to be efficient at blocking cell proliferation in vitro, however, we investigated the biotin-based series using a genetic approach that uses RNA interference (RNAi) and the t-distributed stochastic neighbour embedding (t-SNE) dimensionality reduction to highlight a potential mechanism of action which can guide future efforts to potentiate this mechanism and build more efficient metallodrugs.

Experimental

General procedure for complexes' synthesis

$[(\eta^6\text{-}p\text{-cym})RuCl_2]_2$, $[(\eta^6\text{-}p\text{-cym})OsCl_2]_2$, $[(\eta^6\text{-}p\text{-cym})Ru(1,10\text{-phenanthroline})Cl]PF_6$ (RuPhen), $[(\eta^6\text{-}p\text{-cym})Os(1,10\text{-phenanthroline})Cl]PF_6$ (OsPhen), and 1,10-phenanthroline-5-carboxylic acid were synthesized according to the literature [30–34]. All spectral characterizations (^{1}H and ^{13}C NMR, IR, MS and UV–Vis) and HPLC–UV purities of complexes are reported in the supporting information file.

Synthesis of 1,10-phenanthroline-5-hexanoate-biotinamide (ligand PhBio)

1,10-Phenanthroline-5-carboxylic acid (1 equiv.; 0.30 mmol) was solubilized in 5 mL of DMF with HBTU (1.2 equiv., 0.35 mmol) and DIPEA (3 equiv., 0.90 mmol) and the mixture stirred for 1 h at room temperature until the solution turned dark brown. *N*-(Hexanol)biotinamide (1.2 equiv., 0.35 mmol) was then added to the reaction and stirred overnight. DMF was evaporated under vacuum and the residue washed with 100 mL H_2O. The white residue was filtered through a glass wool plug with cold Et_2O, and vacuum-dried to afford the desired product in 52% yield. ^{1}H NMR (400 MHz, DMSO-d_6): δ (ppm) 9.23–9.22 (Ha, d; 1H, $J = 1.8$ Hz), 9.21–9.20 (Hb, d, 1H, $J = 1.9$ Hz), 9.16–9.15 (Hd, dd, 1H, $J1 = 1.8$ Hz, $J_2 = 4.3$ Hz), 8.72–8.69 (Hc, dd, 1H, $J_1 = 1.8$ Hz, $J_2 = 8$ Hz), 8.70 (He, s, 1H, $J = 1.5$ Hz), 7.87–7.83 (Hfg, mult, 2H), 7.76–7.73 (NH, t, 1H, $J = 5.9$ Hz), 6.40 (NH, s, 1H), 6.34 (NH, s, 1H) 4.44–4.41 (Hh, t, 2H, $J = 6.6$ Hz), 4.29–4.26 (Hm, mult, 1H), 4.11–4.08 (Hn, mult, 1H), 3.09–3.01 (Hki, massif, 3H), 2.80–2.76 (Hl, dd, 1H, $J_1 = 7.4$ Hz, $J_2 = 13.8$ Hz), 2.55–2.53 (Hl, d, 1H, $J = 11.2$ Hz), 2.05–2.01 (Hj, t, 2H, $J = 7.4$ Hz), 1.84–1.77 (Hi, quint, 2H, $J = 7.1$ Hz), 1.63–1.21 (H aliphatic, massif, 14H), ^{13}C NMR (101 MHz, DMSO-d_6): δ (ppm) 172.37, 166.38, 163.22, 152.84, 150.70, 147.32, 146.13, 138.29, 134.57, 132.21, 127.10, 126.29, 126.19, 124.52, 124.23, 65.90, 61.57, 59.71, 55.96, 38.74, 35.76, 29.56, 28.74, 28.67, 28.57, 26.58, 25.87, 25.74. IR (cm^{-1}): 3300, 3205, 2936, 2855, 1731, 1674, 1634. ESI–MS (positive mode) for $C_{29}H_{35}N_5O_4S$ $[M\text{-}H]^+$, calculated m/z 550.2483; found 550.2482 $[M\text{-}H]^+$ (0.05 ppm).

Synthesis of [Ru(p-cym)(PhBio)Cl]PF$_6$ (RuPhBio)

A solution of the Bio ligand (2 equiv; 1.48 mmol) in 1 mL EtOH was added to a solution of $[(\eta^6\text{-}p\text{-cym})RuCl_2]_2$ (1 equiv., 0.74 mmol) in 3 mL MeOH, and the mixture was stirred at reflux overnight under argon. A solution of NH_4PF_6 (3 equiv., 2.22 mmol) in 2 mL EtOH was added, and the solvent removed under reduced pressure. The residue was sonicated in ethanol to give a bright yellow suspension. The yellow solid was recovered by filtration, washed with cold Et_2O, and air-dried. The residue was purified on a neutral alumina column (DCM-MeOH gradient 9:1) to afford the desired product with 61% yield. ^{1}H NMR (400 MHz, DMSO-d_6): δ (ppm) 10.05–10.01 (Hab, dd; 2H, $J_1 = 6.3$ Hz, $J_2 = 9$ Hz), 9.53–9.51 (Hd, d; 1H, $J = 11$ Hz), 9.16–9.13 (Hc, d, 1H, $J = 10.7$ Hz), 9.00 (He, s, 1H), 8.27–8.22 (Hfg, dd, 2H, $J_1 = 5.4$ Hz, $J_2 = 10.4$ Hz), 7.82 (NH, t, 1H, $J = 6.3$ Hz), 6.42 (NH, bs, 2H), 6.38–6.36 (Hc', d, 2H, $J = 5.7$ Hz), 6.14–6.12 (Hd', d, 2H, $J = 7$ Hz), 4.47–4.43 (Hh, t, 2H, $J = 7.7$ Hz), 4.31–4.25 (Hm, mult, 1H), 4.15–4.08 (Hn, mult, 1H), 3.17–3.15 (Hk, d, 1H), 3.11–2.98 (Hi, mult, 2H), 2.82–2.76 (Hl, dd, 1H, $J_1 = 6$ Hz, $J_2 = 15.4$ Hz), 2.66–2.57 (Hl, mult, 1H, $J = 9$ Hz), 2.17 (He', s, 3H), 2.06–2.02 (Hj, t, 2H, $J = 9$ Hz), 1.82–1.78 (t, 2H, $J = 8.7$ Hz), 1.63–1.08 (12H), 0.93–0.90 (Ha', d, 6H, $J = 8.7$ Hz) ^{13}C NMR (101 MHz, DMSO-D_6): δ (ppm) 172.42, 165.13, 163.26, 158.43, 156.96, 147.00, 145.98, 140.78, 137.77, 132.72, 128.88, 128.33, 127.40, 127.20, 109.68, 104.92, 103.38, 86.61, 84.62, 84.52, 66.54, 61.59, 59.73, 56.01, 38.70, 35.78, 30.95, 29.57, 28.78, 28.62, 26.57, 25.93, 25.68, 22.26, 22.22, 18.77. IR (cm^{-1}): 3330, 3130, 3046, 2930, 2861, 1683–1631, 1403. ESI–MS (positive mode) for $C_{39}H_{49}N_5O_4ClRuS$, calculated m/z 820.2239 $[M\text{-}H]^+$; found 820.2243 $[M\text{-}H]^+$ (0.57 ppm). HPLC–UV purity: 95.3 ± 0.1%.

Synthesis of [Os(p-cym)(PhBio)Cl]PF$_6$ (OsPhBio)

A solution of the Bio ligand (2 equiv; 1.48 mmol) in 1 mL EtOH was added to a solution of $[(\eta^6\text{-}p\text{-cym})OsCl_2]_2$ (1 equiv., 0.74 mmol) in 3 mL MeOH, and the mixture was stirred at reflux overnight under argon. A solution of NH_4PF_6 (3 equiv., 2.22 mmol) in 2 mL EtOH was added, and the solvent removed under reduced pressure. The residue was sonicated in ethanol to give a bright yellow suspension. The yellow solid was recovered by filtration, washed with cold Et_2O, and air-dried. The residue was purified on a neutral alumina column (DCM-MeOH gradient 9:1) to afford the desired product with 53% yield. ^{1}H NMR (400 MHz, DMSO-d_6): δ (ppm) 10.01–9.98 (Hab, t; 2H, $J = 8$ Hz), 9.53–9.50 (Hd, d, 1H, $J = 11.1$ Hz), 9.16–9.14 (Hc, d, 1H, $J = 11.2$ Hz), 9.06 (He, s, 1H), 8.24–8.20 (Hfg, mult, 2H, $J_1 = 7.1$ Hz, $J_2 = 11.1$ Hz), 7.84–7.80 (NH, t, 1H; $J = 7.8$ Hz), 6.61–6-59 (Hc', d, 2H, $J = 8$ Hz), 6.42 (NH, s, 1H), 6.37 (NH, s, 1H), 6.33–6.31 (Hd', d, 2H, $J = 8$ Hz), 4.48–4.44 (Hh, t, 2H, $J = 6.6$ Hz), 4.30–4.24 (Hm, mult, 1H, $J_1 = 6.7$ Hz, $J_2 = 10.4$ Hz), 4.12–4.08 (Hn, mult, 1H), 3.11–2.98 (Hki, massif, 3H), 2.81–2.75 (Hl, dd, 1H, $J_1 = 5.7$ Hz, $J_2 = 16$ Hz), 2.57 (Hl, mult, 1H), 2.22 (He', s, 3H), 2.06–2.01 (Hj, t, 2H,

$J = 9.5$ Hz), 1.86–1.77 (t, 2H, $J = 10.2$ Hz), 1.65–1.13 (12H), 0.85–0.83 (Ha', d, 6H, $J = 9.2$ Hz) ^{13}C NMR (101 MHz, DMSO-D_6) δ (ppm) 172.42, 165.07, 163.25, 158.25, 156.85, 148.06, 147.12, 141.00, 138.06, 137.90, 132.99, 129.10, 128.59, 128.11, 128.04, 127.52, 96.20, 95.72, 78.23, 75.07, 74.94, 66.58, 61.59, 59.73, 56.00, 38.70, 35.77, 31.06, 29.57, 28.78, 28.61, 26.57, 25.93, 25.68, 22.49, 18.69. IR (cm^{-1}): 3420, 3163, 3046, 2930, 2861, 1693–1631, 1404. ESI–MS (positive mode) for $C_{39}H_{49}N_5O_4ClOsS$, calculated m/z 902.2754 $[M-H]^+$; found 902.2719 $[M-H]^+$ (3.94 ppm). HPLC–UV purity: 95.7 ± 0.4%.

Synthesis of ligand N-(2-morpholinoethyl)-1,10-phenanthroline-5-carboxamide (ligand PhAEM)

1,10-Phenanthroline-5-carboxylic acid (1 equiv.; 0.89 mmol) was solubilized in 5 mL of DMF with HATU (1.2 equiv., 1.07 mmol) and DIPEA (3 equiv., 2.67 mmol), and the mixture was stirred for 1 h at room temperature until the solution turned dark brown. 4-(2-Aminoethyl)morpholine (1.2 equiv., 1.07 mmol) was then added to the reaction and stirred overnight. DMF was evaporated under vacuum and the residue washed with 100 mL H_2O. The white residue was filtered through a glass wool plug with cold Et_2O, and vacuum-dried to afford the desired product with 72% yield. ^{1}H NMR (400 MHz, DMSO-d_6): δ (ppm) 9.18–9.15 (Hab, dd; 2H), 9.06–9.03 (NH, t, 1H), 8.81–8.78 (Hd, dd, 1H), 8.60–8.58 (Hc, dd, 1H), 8.22 (He, s, 1H), 7.89–7.82 (Hfg, mult, 2H), 3.78–3.73 (O–CH_2, mult, 4H), 8H morpholine in HDO d ^{13}C NMR (101 MHz, DMSO-D_6): δ (ppm) 167.69, 151.21, 150.15, 145.45, 137.14, 134.67, 132.20, 126.93, 126.51, 125.67, 124.09, 123.50, 63.58, 55.27, 51.57, 34.12. IR (cm^{-1}): 3414, 1654–1651, 1548 ESI–MS (positive mode) for $C_{19}H_{20}N_4O_2$ $[M-H]^+$, calculated 337.1659 m/z; found 337.1661 $[M-H]^+$ (0.52 ppm).

Synthesis of [Ru(p-cym)(PhAEM)Cl]PF_6 (RuPhAEM)

A solution of PhAEM ligand (2 equiv.; 1.48 mmol) in 1 mL MeOH was added to a solution of $[(\eta^6\text{-}p\text{-cym})RuCl_2]_2$ (1 equiv., 0.74 mmol) in 3 mL MeOH, and the mixture was stirred at reflux overnight under argon. The solution was filtered through a glass wool plug and the solvent volume was reduced to 2 mL by evaporation. A solution of NH_4PF_6 (3 equiv., 2.22 mmol) in 2 mL MeOH was added, and the solvent removed under reduced pressure. The residue was sonicated in ethanol to give a bright-yellow suspension. The yellow solid was recovered by filtration, washed with cold Et_2O, and air-dried to afford the desired product with 84% yield. ^{1}H NMR (400 MHz, DMSO-d_6): δ (ppm) 9.98–9.96 (Hab, dd; 2H, $J_1 = 1.32$ Hz, $J_2 = 5.38$ Hz), 9.20 (NH, t, 1H, $J = 4.8$ Hz), 9.06–9.04 (Hd, dd, 1H, $J_1 = 1.1$ Hz, $J_2 = 8.5$ Hz), 8.98–8.96 (Hc, dd, 1H, $J_1 = 1.2$ Hz, $J_2 = 8.6$ Hz), 8.48 (He, s, 1H), 8.18–8.14 (Hfg, mult, 2H, $J_1 = 5.3$ Hz, $J_2 = 8.2$ Hz), 6,33–6.31 (Hc', d, 2H, $J = 6.5$ Hz), 6.09–6.07 (Hd', d, 2H, $J = 6.6$ Hz), 4.00–3.17 (H ethyl-morpholine, massif, 12H), 2.64–2.60 (Hb', hept, 1H, $J = 6.6$ Hz), 2.14 (He', s, 3H), 0.88–0.86 (Ha', d, 6H, $J_1 = 2.2$ Hz, $J_2 = 6.8$ Hz) IR (cm^{-1}): 3416, 2977, 1656,1651, 1548. ^{13}C NMR (101 MHz, DMSO-d_6) δ (ppm) 166.73, 157.62, 156.98, 146.11, 145.86, 139.79, 137.89, 129.12, 128.15, 127.58, 127.04, 104.72, 103.62, 86.71, 86.58, 84.37, 63.91, 51.95, 30.93, 22.24, 22.15, 18.79. ESI–MS (positive mode) for $C_{29}H_{34}ClN_4O_2Ru$ $[M-H]^+$, calculated 607.1413 m/z; found 607.1412 $[M-H]^+$ (0.17 ppm). HPLC–UV purity: 97.6 ± 0.1%.

Synthesis of [Os(p-cym)(PhAEM)Cl]PF_6 (OsPhAEM)

A solution of PhAEM ligand (2 equiv.; 1.48 mmol) in 1 mL MeOH was added to a solution of $[(\eta^6\text{-}p\text{-cym})OsCl_2]_2$ (1 equiv., 0.74 mmol) in 3 mL MeOH, and the mixture was stirred at reflux overnight under argon. The solution was filtered through a glass wool plug, and the solvent volume was reduced to 2 mL by evaporation. A solution of NH_4PF_6 (3 equiv., 2.22 mmol) in 2 mL MeOH was added, and the solvent removed under reduced pressure. The residue was sonicated in ethanol to give a bright-yellow suspension. The yellow solid was recovered by filtration, washed with cold Et_2O, and air-dried to afford the desired product with 57% yield. ^{1}H NMR (400 MHz, DMSO-d_6): δ (ppm) 9.98–9.96 (Hab, dd; 2H, $J_1 = 1.2$ Hz, $J_2 = 4.9$ Hz), 9.20 (NH, t, 1H, $J = 5$ Hz), 9.06–9.04 (Hd, dd, 1H, $J_1 = 1.2$ Hz, $J_2 = 8.5$ Hz), 8.98–8.96 (Hc, dd, 1H, $J_1 = 1.6$ Hz, $J_2 = 8.4$ Hz), 8.48 (He, s, 1H),8.18–8.14 (Hfg, mult, 2H, $J_1 = 5.1$ Hz, $J_2 = 8.1$ Hz), 6,33–6.31 (Hc', d, 2H, $J_1 = 2.2$ Hz, $J_2 = 5.2$ Hz), 6.09–6.07 (Hd', d, 2H, $J_1 = 2.2$ Hz, $J_2 = 5.2$ Hz), 4.00–3.17 (H ethyl-morpholine, massif, 12H), 2.64–2.60 (Hb', hept, 1H $J = 1.8$ Hz), 2.14 (He', s, 3H), 0.88–0.86 (Ha', d, 6H, $J_1 = 2.7$ Hz, $J_2 = 6.9$ Hz). ^{13}C NMR (101 MHz, DMSO-d_6) δ 156.89, 147.22, 147.01, 140.03, 129.36, 128.42, 128.20, 128.06, 127.68, 95.56, 78.31, 78.21, 74.84, 74.81, 63.92, 55.59, 51.95, 31.05, 22.49, 22.42, 18.70. IR (cm^{-1}): 3414, 2956 1655, 1651, 1548 ESI–MS (positive mode) for $C_{29}H_{34}ClN_4O_2Os$ $[M-H]^+$, calculated 698.1899 m/z; found 698.19895 $[M-H]^+$ (0.50 ppm). HPLC–UV purity: 95.8 ± 0.1%.

Synthesis of [Ru(p-cym)(AEM)Cl]PF_6 (RuAEM)

A solution of 4-(2-aminoethyl)morpholine (2 equiv.; 0.32 mmol) in 1 mL MeOH was added to a solution of $[(\eta^6\text{-}p\text{-cym})RuCl_2]_2$ (1 equiv., 0.16 mmol) in 3 mL MeOH, and the mixture was stirred at reflux overnight under argon. The solution was filtered through a glass wool plug, and the solvent volume was reduced to 2 mL by evaporation. A

solution of NH_4PF_6 (3 equiv., 0.48 mmol) in 2 mL MeOH was added, and the solvent removed under reduced pressure. The yellow solid was recovered by recrystallized with hot MeOH to afford the desired product with 78% yield. ^{1}H NMR (400 MHz, DMSO-d_6): δ (ppm) 6.28–6.26 (NH, d; 1H, J = 9.7 Hz), 5.87–5.85 (Hc', d; 1H, J = 6.6 Hz), 5.79–5.78 (Hc', d, 1H, J = 6.6 Hz), 5.31–5.51 (Hd', d, 1H, J = 6.6 Hz), 5.38–5.36 (Hd', d, 1H, J = 6.6 Hz), 4.14–4.08 (H morpholine, t, 1H, J_1 = 2.7 Hz, J_2 = 11.8 Hz), 3.99–3.94 (Ha, mult, 2H), 3.80–3.66 (H morpholine, mult, 2H,), 3.50–3.45 (Hb, t, 2H, J = 7.6 Hz), 3.40–3.37 (H morpholine, d, 1H, J = 11.8 Hz), 3.05–3.02 (H morpholine, d, 1H, J = 13.2 Hz), 2.95–2.89 (Hb', hept, 1H, J = 6.5 Hz), 2.75–2.56 (H morpholine, massif, 2H), 2.22 (He', s, 3H), 2.09–2.02 (H morpholine, dt, 1H, J_1 = 3.5 Hz, J_2 = 12.2 Hz), 1.26–1.20 (Ha', dd, 6H, J_1 = 6.7 Hz, J_2 = 14.7 Hz) ^{13}C NMR (101 MHz, MeOD): δ (ppm) 107.03, 95.57, 86.17, 82.73, 80.91, 79.45, 62.02, 61.37, 61.16, 60.19, 50.69, 42.60, 30.83, 21.35, 20.98, 16.53. IR (cm^{-1}): 3351, 3340, 2963, 2823, 1693, 1595, 1473, 1450.5 ESI–MS (positive mode) for $C_{16}H_{28}ClN_2ORu$ $[M\text{-}H]^+$, calculated 401.0929 m/z; found 401.0935 $[M\text{-}H]^+$ (1.6 ppm). HPLC–UV purity: 97.6 ± 0.1%.

Synthesis of [Os(p-cym)(AEM)Cl]PF$_6$ (OsAEM)

A solution of 4-(2-aminoethyl)morpholine (2 equiv.; 0.32 mmol) in 1 mL MeOH was added to a solution of [(η^6-*p*-cym)$OsCl_2$]$_2$ (1 equiv., 0.16 mmol) in 3 mL MeOH, and the mixture was stirred at reflux overnight under argon. The solution was filtered through a glass wool plug, and the solvent volume was reduced to 2 mL by evaporation. A solution of NH_4PF_6 (3 equiv., 0.48 mmol) in 2 mL MeOH was added, and the solvent removed under reduced pressure. The yellow solid was recovered by recrystallized with hot MeOH to afford the desired product with 48% yield. ^{1}H NMR (400 MHz, DMSO-D_6): δ (ppm) 6.84–6.82 (NH, d, 1H, J = 10.2 Hz), 6.15–6.14 (Hd', d, 1H, J = 6.1 Hz), 6.07–6.06 (Hd', d, 1H, J = 6.1 Hz) 5.81–5.80 (Hc', d; 1H, J = 6.1 Hz), 5.68–5.66 (Hc', d, 1H, J = 6.1 Hz), 4.64–4.62 (H morpholine, quint, 1H, J = 5.4 Hz), 4.06–3.92 (H morpholine, massif, 2H), 3.82–3.76 (H morpholine, t, 1H, J = 12.4 Hz), 3.63–3.59 (H morpholine, td, 1H, J_1 = 4.1 Hz, J_2 = 13.6 Hz), 3.45–3.42 (H morpholine, d, 2H, J = 12.4 Hz), 3.12–3.08 (H morpholine, d, 1H, J = 13.7 Hz), 2.78–2.76 (Hb', hept, 1H, J = 7 Hz), 2.70–2.34 (H morpholine, massif, 3H), 2.22 (He', s, 3H), 1.20–1.18 (dd, 6H, J_1 = 5.6 Hz, J_2 = 6.9 Hz) ^{13}C NMR (101 MHz, DMSO-D_6): δ (ppm) 97.60, 85.82, 79.97, 73.75, 71.48, 70.76, 62.23, 62.06, 61.36, 52.40, 45.06, 30.72, 30.69, 23.30, 22.07, 17.90. IR (cm^{-1}): 3324, 3258, 2973, 2880, 1693, 1599, 1472, 1447 ESI–MS (positive mode) for $C_{16}H_{28}ClN_2OOs$ $[M\text{-}H]^+$, calculated 489.1469 m/z; found 489.1473 $[M\text{-}H]^+$ (1.4 ppm). HPLC–UV purity: 97.2 ± 0.3%.

Computational details

All quantum mechanical calculations have been achieved using Orca 4.2.1. Geometries of the investigated systems were fully optimized at the spin-restricted density functional theory level using the dispersion-corrected ωB97x-D exchange–correlation (XC) functional [35]. The balanced polarized triple-zeta basis set def2-TZVP from Ahlrichs et al. [36, 37] has been used for all atoms. TDDFT was performed using the same XC functional and basis set but the calculations were sped up using the Resolution of Identity (RI) approximations for Coulomb integrals and the COSX numerical integration for HF exchange (RIJCOSX). Second-order Møller–Plesset (MP2) calculations used the RI approximation for the MP2 correlations integrals. To account for an accurate description of relativistic effects on the core electrons, an all-electron scalar relativistic approximation (the zeroth order regular approximation, ZORA) was used [38]. Potential energy surface minima found upon optimization were confirmed by frequency calculations and free energies were corrected to account for the zero-point energy. Optimized geometries were verified as minima (i.e. zero imaginary frequencies). Transition states were further verified as first-order saddle points by frequency calculations (i.e. one imaginary frequency). Natural Bond Orbital (NBO) analysis was performed using the latest version of the program from Weinhold and co-workers (NBO7) [39].

Cytotoxicity profiles (MTT assay)

The growth inhibitory potency of the six compounds was determined using a colorimetric MTT assay. Gliomas Hs683 (ATCC, code HTB-138), non-small cell lung cancer A549 (DSMZ, code ACC107), human breast adenocarcinoma MCF7 (ATCC, code HTB-22), human glioblastoma U373 (ATCC, code HTB-17) and murine melanoma B16F10 (ATCC, code CRL-647) cell lines were used. All of the cell lines were maintained under a special atmosphere (37 °C, 5% CO_2) in RPMI1640 supplemented with heat-inactivated (56 °C, 1 h) fetal bovine serum (10%), glutamine (2%), penicillin–streptomycin (2%) and gentamicin (0.2%); all of these reagents were purchased from Lonza. The cells were seeded in 96-microwell plates (the seeding density varied between 800 and 1200 cells in 100 µL/well, depending on the cell line) 24 h before treatment to ensure adequate cell adhesion. The compounds were assayed from 3 µM up to 300 µM for 72 h (from 30 mM stock solutions in DMSO); the cell population growth in the control and treated samples was determined according to the capability of living

cells to reduce the MTT yellow product (0.5 mg/mL in white RPMI1640 medium; 100 µL/well) during a minimum of 3 h into formazan blue crystals in their mitochondria. After removing of the MTT solution and centrifugation at 200 rpm for 8 min, the crystals are solubilized in DMSO (100 µL/well). The cells surviving after 72 h of culture in the presence or absence of the various compounds is directly proportional to the intensity of the blue color. The optical density was measured with a Biorad Model 680XR reader at 570 nm (with a reference of 630 nm). Control cells were treated with the highest concentration of DMSO (1%) and no difference in term of viability was observed between cells treated with 1% DMSO and untreated cells. Each experiment was repeated three times.

Crystal structure determination and refinement

Suitable crystals for structure determination were obtained for the Ru^{II} and Os^{II} complexes, giving red–orange plate like crystals after crystallization in methanolic solutions. Diffraction data was collected on a MAR345 image plate using Mo Kα radiation generated by a Rigaku Ultra X18S rotating anode (Xenocs FoX3D mirrors). The collected images were integrated and reduced by CrysAlisPRO and the implemented absorption correction was applied. Structure was solved by SHELXT and refined by full-matrix least squares against F2 using SHELXL 2014/7.

Cellular uptake

Approximately 10^6 cells were seeded in 60 mm × 10 mm T25 flasks and incubated for 24 h. Cells were then treated with the cytotoxic agent at 10 µM and incubated for 24 h at 37 °C in 5% CO_2. Culture medium was then removed, the cells washed with trypsin (3 × 1 mL) and harvested by trypsinization (1 mL). Cell-containing suspensions were centrifuged at 1200 rpm for 5 min (25 °C) and the cell pellets were resuspended in 100 µL of 70% HNO_3. The suspensions were digested at 60 °C for 1 h. 400 µL of a metal-stabilizing aqueous solution (acetic acid 0.05% v/v, thiourea 0.01 M and ascorbic acid 0.1 g/L) was then added to the samples to avoid the release of the volatile and toxic OsO_4 [40, 41]. Ru and Os concentrations in all samples were determined with a quadrupole inductively coupled plasma mass spectrometry (ICP-MS) Agilent 7700, where indium (In) was used as internal standard for correcting the instrumental drift. Each experiment was repeated three times.

Reactions with bionucleophiles

Mass spectrometry was performed on an Agilent Q-TOF-6520 system; m/z from 100 to 1700 were recorded in positive mode. 500 µM solutions of the complexes were reacted with silver ($AgPF_6$, 1.5 equiv) in milliQ water for 24 h at 37 °C. The samples were then incubated at 37 °C for another 24 h after the addition of GSH (10 equiv.) or 9MeG (10 equiv.). For aquation, samples were kept unchanged for another 24 h at 37 °C. Samples were diluted to 5 µM in a mixture of 0.2% formic acid in water/acetonitrile (2:8) before injection.

shRNA signatures [42–44]

For the preparation of shRNA viral vectors, phoenix cells (Human Embryonic Kidney 293T) were used for transfection. Phoenix cells were cultured in DMEM media containing 10% FBS, 1% Pen-Strep-Glutamine. Eight shRNA plasmids containing GFP and Ψ viral vector were transfected using the calcium phosphate method ($CaCl_2$ stock solution 2 M and Hepes buffer solution). GFP signals were observed 48 h post-transfection with a fluorescence microscope (Evos FL auto-imaging system by Thermofisher) to confirm the presence of at least 50% of GFP-positive cell population. Media was changed after 24 h and 48 h, just before infection of mice lymphoma cells (Eμ-Myc). Eμ-Myc were cultivated in 50:50 DMEM-IMDM media containing 10% FBS, 1% Pen-Strep-Glutamine and 55 µM of 2-mercaptoethanol. shRNA viral vectors were purified and concentrated (before infection) with polybrene and chondroitin sulfate (80 µg/mL) [45]. After centrifugation (10,000 rpm, 5 min), supernatant was removed and viral pellets were re-dissolved in 500 µL of fresh media (DMEM-IMDM-FBS 2.5%-BME 55 µM-1%Pen-Strep-Glu). Eμ-Myc were then seeded in 10 cm dishes and 6 wells/plate at 10^5 cells/mL in media (DMEM-IMDM-FBS 2.5%-BME 55 µM-1%Pen-Strep-Glu) and infected with purified shRNA viral vectors (volumes vary depending on the shRNA viral vector). The remaining viral solutions (400 µl) were stocked with a 1:1 mixture of glycerol and Eμ-Myc (400 µL; vol total = 800 µL) media and stored at – 20 °C for future use. After 48 h, the supernatant containing the virus was removed after spin-down (500 rpm, 5 min, r.t.) and pellets were washed twice by PBS. Infected Eμ-Myc cells were then seeded in 10 cm dishes and infection % (between 10 and 20% GFP-positive cell population depending on the shRNA viral vector, controls are shown in SI Figure S13) as determined by flow cytometry on a BD Accuri C6 Plus. Before the shRNA signatures experiment, IC_{50}, IC_{80} and IC_{90} for 48 h were determined for compounds RuPhBio and OsPhBio, cisplatin and doxorubicin on wild-type Eμ-Myc cell line with propidium iodide as viability marker by flow cytometry. For the shRNA signature experiment, Eμ-Myc cells were seeded in 10 cm dishes at 10^5 cells/mL and treated at three different at IC_{80}, IC_{85} and IC_{90} for 72 h in triplicate and analyzed by flow cytometry with propidium iodide (PI) at 10 µg/mL to determine of resistance index (RI). RI was calculated with the following equation

(G1 = GFP % of the untreated GFP+/PI− population; G2 = GFP % of the treated GFP+/PI− population):

$$RI = (G2 - (G1 \times G2))/(G1 - (G1 \times G2)).$$

Classifications are predicted by analysis of $\log_2 RI$ by K-nearest neighbors (KNN) and principal component analysis (PCA) with the R program. Cisplatin and doxorubicin were used as positive control and were correctly classified as DNA cross-linking agents and topoisomerases II inhibitors, respectively.

Results

Synthesis

We prepared three different series of the Ru/Os metal–arene complexes, namely the AEM, PhAEM and PhBio series. They were synthesized from the dimeric metal precursors $[M(p\text{-cymene})Cl_2]_2$, where M is either Ru or Os, and is complexed to the three different ligands (AEM, PhAEM and PhBio). The PhAEM and PhBio series were prepared as follows: (1) the 1,10-phenanthroline-5-carboxylic acid was either functionalized using an amide with 4-(2-aminoethyl) morpholine (ligand PhAEM, Fig. 1A) or an ester linkage with the N-(hexanol)biotinamide (ligand PhBio, Fig. 1A) and (2) chelated to the metal dimer precursors (Fig. 1B). The AEM series was obtained by direct chelation of the N,N-bidendate 4-(2-aminoethyl)morpholine ligand (Fig. 1B). All six complexes were characterized by ^{1}H NMR, ^{13}C NMR, IR and MS (SI.2).

Crystal structures

Single crystals were grown from oversaturated RuAEM and OsAEM hot methanolic solutions and were analyzed by X-ray diffraction. Crystallographic parameters for these compounds are given in SI (Table S1) while selected interatomic distances (Å) and angles (deg) from the crystal structures are detailed in Table 1. As expected, the coordination spheres of RuAEM and OsAEM are formed by the η^6-*p*-cymene, a chloride and the N,N-bidendate 4-(2-aminoethyl)morpholine ligand. Both X-ray structures

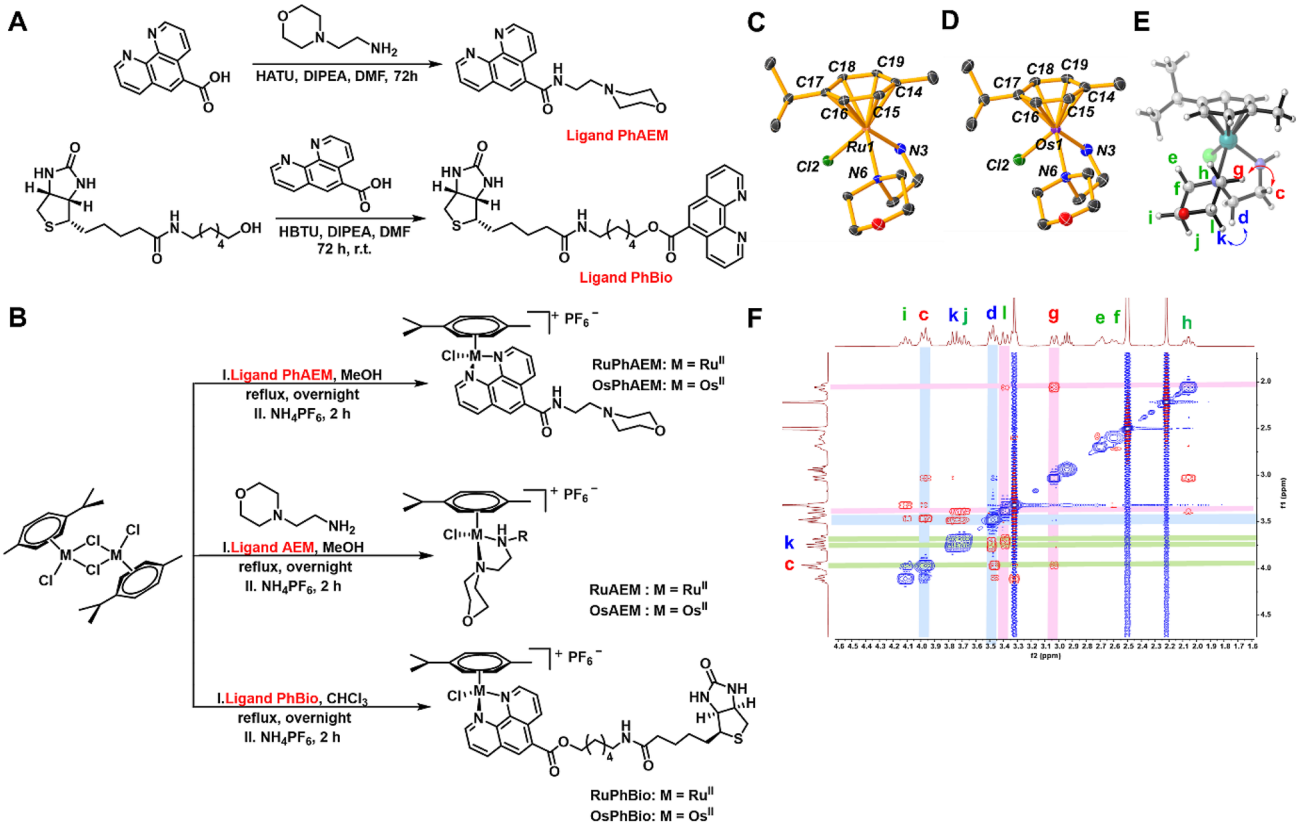

Fig. 1 **A** Synthesis of the PhAEM and PhBio ligands by standard coupling methods. **B** Synthesis of the three series of Ru^{II} and Os^{II} organometallic complexes: PhAEM, AEM and PhBio. X-ray crystal structures of the cationic RuAEM (**C**) and OsAEM (**D**) complexes (thermal ellipsoids at 50% level). Colors are as follows: C, black; N, blue; O, red; Cl, green; Ru, orange; Os, violet (H are omitted for clarity). **E** DFT structure of RuAEM. **F** ROESY for RuAEM and through-space correlations

Table 1 Selected interatomic distances (Å) and angles (deg) from the crystal structures of RuAEM and OsAEM

Interatomic distances (Å)		
	OsAEM	RuAEM
M–Cl2	24.059	24.024
M–N3	2.146	21.329
M–N6	2.218	22.163
M–Centroid$_{arene}$	1.671	1.680
M–C14	2.208	2.209
M–C15	2.189	2.199
M–C16	2.202	2.208
M–C17	2.212	2.216
M–C18	2.189	2.193
M–C19	2.172	2.173
Angles (deg)		
N6–M–N3	79.89	80.27
N6–M–Cl2	85.82	86.82
N3–M–Cl2	81.03	81.87
C14–M–Cl2	157.20	156.36
C17–M–Cl2	89.19	88.84
C14–M–N3	96.62	96.44
C17–M–N3	152.00	152.07
C14–M–N6	116.26	116.27
C17–M–N6	125.74	125.65

are characteristic of the "three-legs piano-stool" configuration with the metal complexes being positively charged and neutralized by a PF_6^- counterion (Fig. 1C, D). Distance range of M–Cl (Ru–Cl 2.402 Å and Os–Cl 2.406 Å), M–N (Ru–N from 2.2163 to 2.209 Å and Os–N from 2.146 to 2.218 Å) and M–CHp-cymene (Ru–CHp-cymene from 2.173 to 2.216 Å and Os–CHp-cymene from 2.172 to 2.212 Å) are in agreement with the similar structures of [Ru(η^6-p-cymene)(ethylenediamine)Cl]PF_6 [33] and [Os(η^6-biphenyl)(ethylenediamine)Cl]PF_6 [32], respectively. Little differences are observed between RuAEM and its Os analogue in terms of bond lengths and angles (N–Ru–N, 80.3° and N–Os–N, 79.9°).

Solution state conformation

To determine the solution state conformation of RuAEM, a 2D-NMR analysis, namely the rotating frame Overhauser enhancement spectroscopy (ROESY), was carried out. Cross-correlations between Hc and Hg, Hd and Hk were observed (Fig. 1E, F), indicating their close proximity, as seen in the crystal structure. This suggests rather similar conformations in solution and in the solid state. In addition, this allowed us to properly assign ^{1}H signals on the morpholine group.

UV–Vis spectroscopy

The absorption spectra for the six complexes are plotted in SI (Figure S1). Ru complexes of the Bio and PhAEM series display similar absorption profiles and this remains true for the osmium analogs. While the RuPhBio and RuPhAEM complexes are characterized by strong absorption bands between 270 and 320 nm, the Os ones display an additional band around 380 nm. Absorption bands observed for the AEM series were less intense due to the absence of the 1,10-phenanthroline ligand. RuAEM shows bands between 270 and 420 nm and its Os analog is characterized by absorption bands between 270 and 350 nm. Experimental UV spectra for each compound are compared with theoretical spectra generated by means of TD-DFT calculations (SI.5.1) to help assign the nature of the transitions, and this was achieved through electron density difference and natural transition orbital (NTO) analysis (SI.5.3). The character of these transitions is, however, not fully elucidated and usually includes a mixture of ligand-to-ligand charge transfer (LLCT), metal to ligand charge transfer (MLCT) and *d–d* transitions. We will consider these mixtures of LLCT and MLCT transitions as metal–ligand to ligand charge transfer (MLLCT) [46]. Attributions for the most important charge transfer transitions for the six complexes are given in SI.5.3. Despite having different ligands, similar charge transfer transitions are calculated across the series. For all compounds, the charge transfer observed at the lowest energy (S2 state) is mostly attributed to a *d–d* transition as well as a small MLLCT contribution. Similarly, the second lowest energy transition (S3 state) results in a mixture of *d–d* transitions and MLLCT, except for OsPhBio for which it comes from MLCT. The third lowest energy charge transfer transitions are similar for compound OsPhBio (S5 state), AEM (S6 state), and PhAEM (S6 and S4 states), combining a mixture of *d–d* transition and MLCT. Absorption bands at higher energies (S19 for RuAEM, S13 and S21 for OsAEM) are assigned to LMCT. For the PhAEM series, S19 for RuPhAEM and S16 for OsPhAEM are characterized by intra-ligand charge transfer transitions (ILCT). We can also see a mixture of LMCT and ILCT for the S24 of RuPhBio.

Frontier molecular orbitals

The highest occupied (HOMO) and lowest unoccupied molecular orbitals (LUMO) are printed in SI (Figure S3). For the AEM series, the HOMO density is spread over the metal center (orbital dxy) and the chloride, whereas the LUMO is mostly localized at the metal center (orbital dx^2-y^2) and the arene moiety with a small contribution of the

chloride ligand. The HOMO/LUMO are more discriminated in the PhAEM series, the occupied orbital being well localized on the lone pair of the nitrogen atom of the morpholine and the LUMO density largely on the 1,10-phenanthroline ligand. The Bio complexes have both the HOMO and LUMO on the phenanthroline region. The order of HOMO–LUMO gaps is as follows: AEM > PhBio > PhAEM, with a small influence of the metal center.

Reactions with bionucleophiles (H_2O, GSH, 9MeG)

Aquation is known to be a major mechanism of activation of metal complexes, particularly for platinum compounds [47, 48]. Ru and Os complexes with halogen ligands are also thought to be activated by a similar mechanism. The simple Ru^{II} 1,10-phenanthroline complex, RuPhen (Fig. 2A), is quickly activated in water to form the aqua complex ($k = 1.8\ h^{-1}$, $t_{1/2} = 22$ min at 37 °C) [49]. In contrast, the Os analog OsPhen is more inert toward hydrolysis ($k = 0.073\ h^{-1}$, $t_{1/2} = 9.45$ h at 45 °C) [32]. We used Ruphen as a comparison for the aquation reaction of the RuAEM compounds. RuPhen and RuAEM differ by the hybridization of the chelating nitrogen, sp^2 for RuPhen and sp^3 for RuAEM. The RuPhen aquation was complete in less than 1 h (Fig. 2A), which is consistent with the published half-life of 22 min [49]. RuAEM was, however, found to be inert to aquation in similar experimental conditions, and the aqua adduct of RuAEM was not observed ^{1}H NMR after 6 h (Fig. 2B). To explain these differences in reactivity, we used DFT and calculated the thermodynamic parameters of the aquation reaction for RuPhenMetA (where the 1,10-phenanthroline ligand is functionalized with methyl amide group on the C5 position, to speed up calculations) and RuAEM (Fig. 2C). Free energies of activation ($\Delta G^{\ddagger}$) calculated for the transition states (TS) at standard conditions for temperature and pressure are about 5 kcal/mol higher for the AEM series compared to the PhenMetA, while the metal accounts for approx. 2 kcal/mol in favor of Ru (Fig. 2D). To extend our theoretical and experimental observations, we calculated the transition states for the Ru and Os complexes bearing an ethylenediamine (en) ligand, namely RuEn and OsEn. Closely related compounds RM175 [Ru(biphenyl)

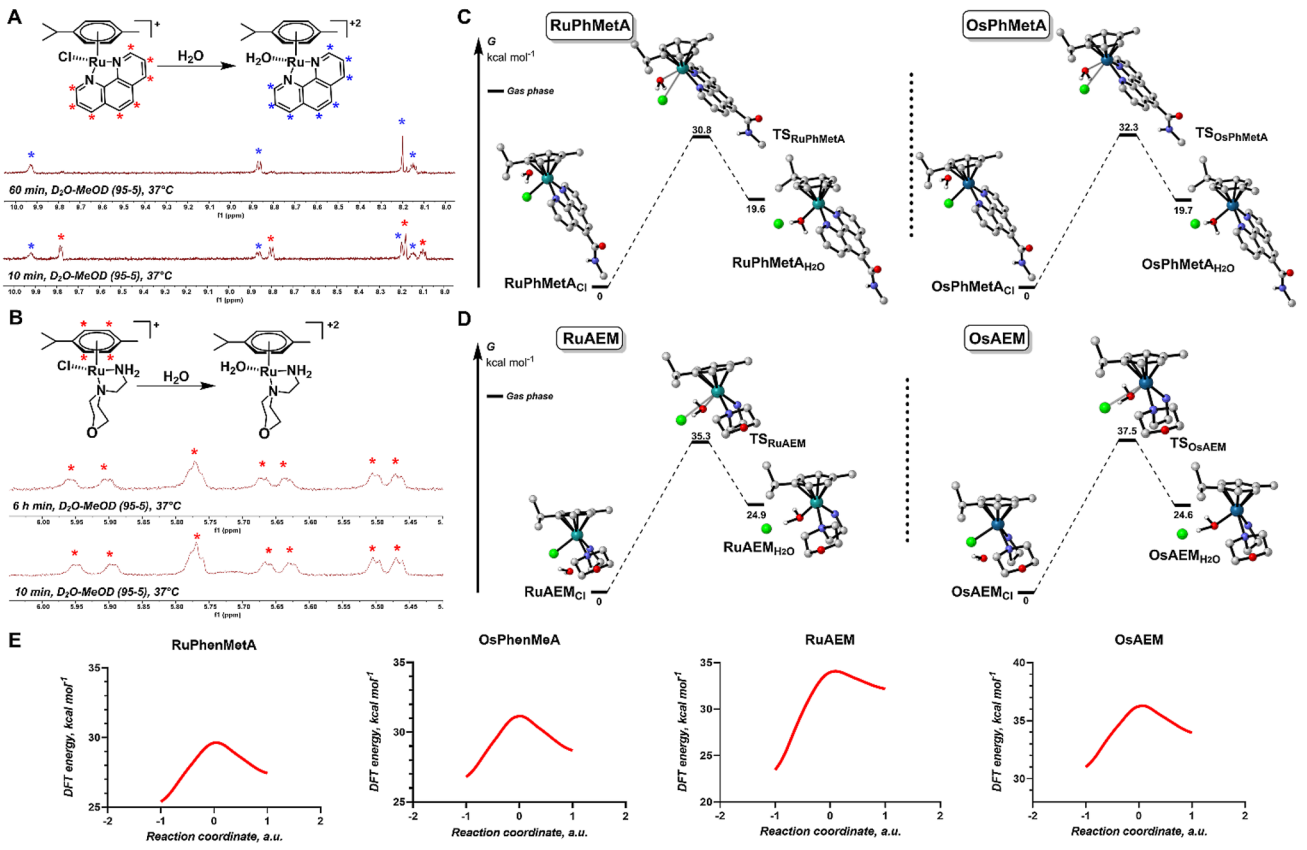

Fig. 2 **A** Aquation reactions followed by ^{1}H NMR for RuPhen at 0.5 mM, in a D_2O-MeOD mixture (95:5) at 37 °C for 1 h. **B** Aquation reaction followed by ^{1}H NMR for RuAEM at 1 mM in a D_2O-MeOD mixture (95:5) at 37 °C for 6 h. **C**, **D** DFT free energy profiles at the ωB97xD/def2-TZVP level of theory for the aquation of compounds RuPhMetA, OsPhMetA, RuAEM and OsAEM. **E** IRC profiles for the aquation of the same four compounds

Cl(en)]$^+$ and its Os analogs undergo rapid aquation at 37 °C with $t_{1/2}$ of 2.9 min and 2.8 h, respectively [32, 50]. Despite having the same type of chelating nitrogen than the AEM compounds (i.e. sp^3), the $\Delta G^{\ddagger}$ for RuEn and OsEn (27.3 and 29.3 kcal/mol) are closer to the PhMetA compounds (30.8 and 32.3 kcal/mol) than the AEM compounds (35.3 and 37.5 kcal/mol). Consequently to these combined experimental and theoretical observations, we suggest that the hybridization of the chelating *N*-donors do not much influence aquation rate but that the morpholine moiety and its tertiary amine are detrimental to the formation of the aqua complex. All the free energy profiles and TS of the aquation reactions represented in Fig. 2C, D were confirmed by intrinsic reaction coordinate (IRC) calculations. Finally, all the aquation reactions are unfavorable under standard conditions, and this is exacerbated for RuAEM and OsAEM (24.9 and 24.6 kcal/mol) in comparison to RuPhMetA and OsPhMetA (19.6 and 19.7 kcal/mol).

We then looked by MS at the formation of aquated complexes as well as the GSH and 9-methylguanine (9MeG) adducts for RuAEM, OsAEM, RuPhen and OsPhen. The latter pair has been used as a substitute for RuPhAEM, OsPhAEM, RuPhBio and OsPhBio due to the similar 1,10-phenanthroline ligand. Expected and observed reaction products are given in Table 2. For RuPhen and OsPhen, we can see a shared reactivity profile with the presence of the aqua products, as well as the GSH and 9MeG adducts. In contrast, the reaction products of RuAEM and OsAEM with bionucleophiles differed from the 1,10-phenanthroline analogs. For the AEM series, the loss of the chlorido was detected but no aqua and GSH reaction products were observed, yet small signals corresponding to the 9MeG adduct were found (Table 2). We also noticed the formation of bimetallic adducts during the aquation and 9MeG reactions for both OsAEM and RuAEM. This may suggest a distinct mode of activation for the AEM and the Phen series: while the RuPhen and OsPhen loosed the chloride ligand and aquated rapidly, aqua forms of RuAEM and OsAEM are being absent. The lack of formation of reactive aqua intermediates may impair the in vitro activity in this series.

Metal–arene charge transfer

Metal–arene coordination is well known to stabilize half-sandwich complexes, and increase lipophilicity [10]. Recent developments further highlighted the importance of the metal–arene: the *p*-cymene can be released to form new complexes via an original pathway [51] and this may play a role in the interaction with proteins [52]. We thus sought to explore the nature of the metal–arene bond. The charge transfer (CT) in metal–arene complexes has received little attention to date, and till now essentially by the means of crystallographic data [53]. We here provide a quantitative description of the metal–arene bonds in our complexes by means of second-order perturbative estimates of donor–acceptor interactions (NBO_{CT}), as implemented in the natural bond orbital (NBO) software. Classical "donor–acceptor bonding" in metal complexes consists in σ-electron donation from the ligand to the metal acceptor followed by π back-donation from the metal to the vacant π* orbital of the ligand. The metal–arene bonding as seen here and in the typical half-sandwich compounds is composed of electron donation from the filled *d* orbitals on the metal to π* antibonding orbitals on the arene. We have quantified these for each complex of the series using a truncated version methyl ester version of the biotin ligand (RuPhMet), then compared the metal–arene distances obtained from the crystal structures to those obtained from DFT (Fig. 3). A common trend is first found among the series: the Os center is a better donor to the arene, which may be expected due to the more diffuse *d* orbitals and this leads to a consistent increase in the CT stabilization of the metal–arene bond of around 25 kcal/mol in comparison to the Ru compounds, for a total CT stabilization of around

Table 2 Observed MS ions for the reactions with bionucleophiles (H_2O, GSH and 9MeG)

	Observed fragments	Experimental (calculated) m/z
Aquation	$[RuAEM - Cl - H]^+$	365.1170 (365.1167)
$- Cl + H_2O$	$[OsAEM - Cl - H]^+$	455.1733 (455.1738)
	$[RuPhen - Cl + H_2O]H^+$	435.0819 (435.0932)
	$[OsPhen - Cl - H + H_2O]^+$	523.1403 (523.1425)
GSH	/	/
− Cl + GSH	/	/
	$[RuPhen - Cl + GS]^+$	722.1585 (722.1586)
	$[OsPhen - Cl + GS]^+$	812.2097 (812.2158)
9-MeG	$[RuAEM - Cl - H - O + 9MeG]^+$	514.0637 (514.1868)
− Cl + 9MeG	$[OsAEM - Cl - H - O + 9MeG]^+$	604.1220 (604.2440)
	$[RuPhen - Cl - H + 9MeG]^+$	580.1407 (580.1399)
	$[OsPhen - Cl - H + 9MeG]^+$	670.1934 (670.1970)

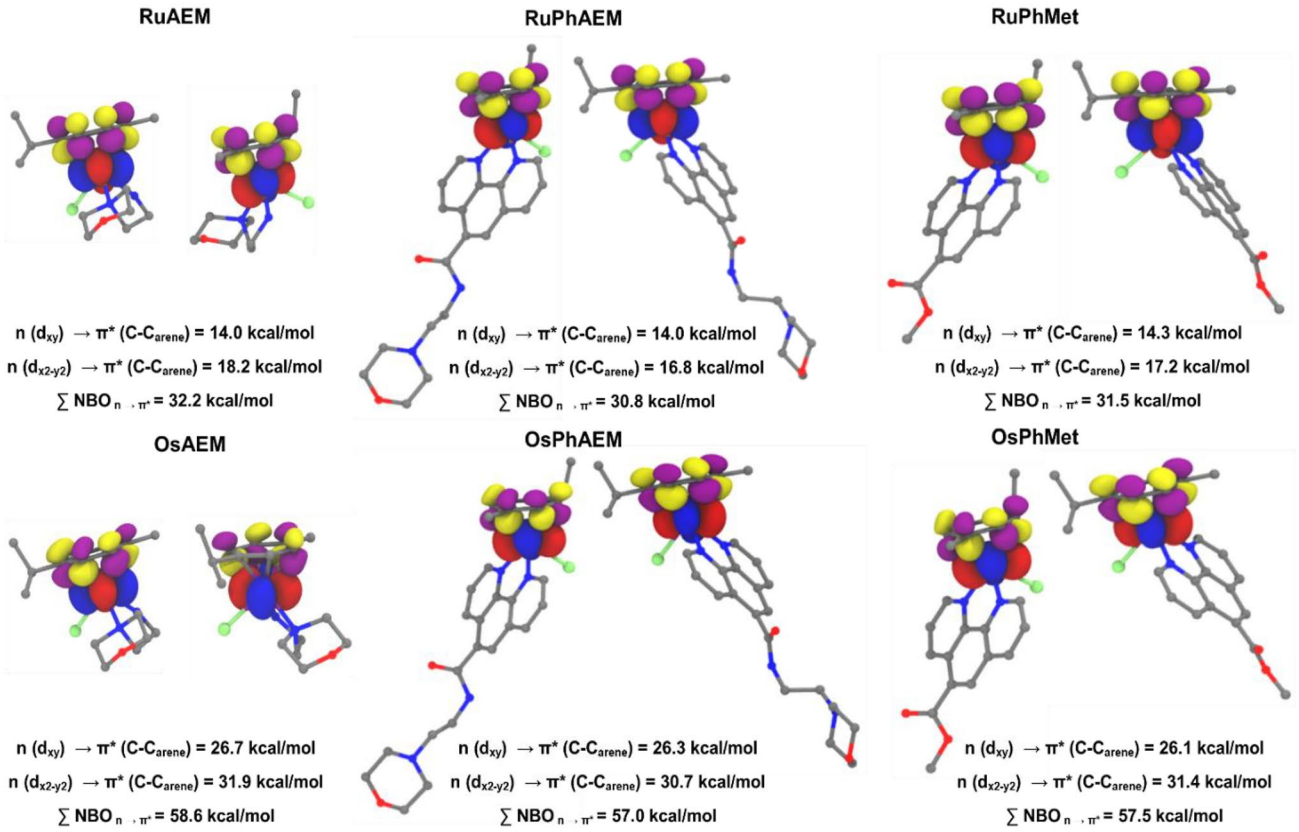

Fig. 3 Metal–arene donor–acceptor delocalizations and their perturbative estimates in the NBO basis at the ωB97xD/def2-TZVP level. Filled *d* orbitals are depicted in blue/red and the antibonding π* orbitals in yellow/purple

30 and 55 kcal/mol for Ru and Os complexes, respectively. This in turn results in a shrunken metal–arene distance in the case of Os, however, this bond length difference is rather small in our RuAEM and OsAEM X-ray structures. Calculations at the MP2 level consistently delivered an increased metal–arene CT for the Os compounds, as does the use of the PBE0 functional. Our results also compare with similar NBO calculations on Ru metal–arene complexes [54].

Cytotoxicity profiles

The in vitro antiproliferative activities of Ru and Os complexes were first determined by MTT assays on five cancer cell lines: the non-small cell lung cancer cell line A549 (human lung carcinoma), MCF-7 (human breast adenocarcinoma), SKMEL28 (human melanoma), U373 (human glioblastoma) and B16F10 (murine melanoma). These cytotoxicity profiles were compared with those of the parent 1,10-phenanthroline compounds RuPhen and OsPhen (Table 3). No strong antiproliferative effects were observed for either series bearing the morpholino ligand (PhAEM and AEM). The IC_{50} for the biotinyl complexes were better but without any improvement of the activity in comparison to the parent phen compounds.

Table 3 In vitro growth inhibition as determined by MTT assays on five cancer cell lines (IC_{50}, μM)

IC_{50} (μM)	A549	MCF-7	U373	B16F10
RuPhBio	167 ± 9	118 ± 10	527 ± 52	392 ± 63
OsPhBio	112 ± 4	77 ± 9	355 ± 70	187 ± 20
RuAEM	436 ± 49	382 ± 24	354 ± 19	367 ± 11
OsAEM	376 ± 58	459 ± 76	290 ± 28	477 ± 28
RuPhAEM	349 ± 14	493 ± 133	276 ± 56	495 ± 80
OsPhAEM	442 ± 48	1587 ± 738	354 ± 53	684 ± 105
RuPhen	65 ± 13	75 ± 4	99 ± 14	71 ± 16
OsPhen	83 ± 1	73 ± 5	247 ± 37	147 ± 13
Cisplatin	1.7 ± 0.2	8.7 ± 0.6	3.7 ± 0.2	9.4 ± 0.7

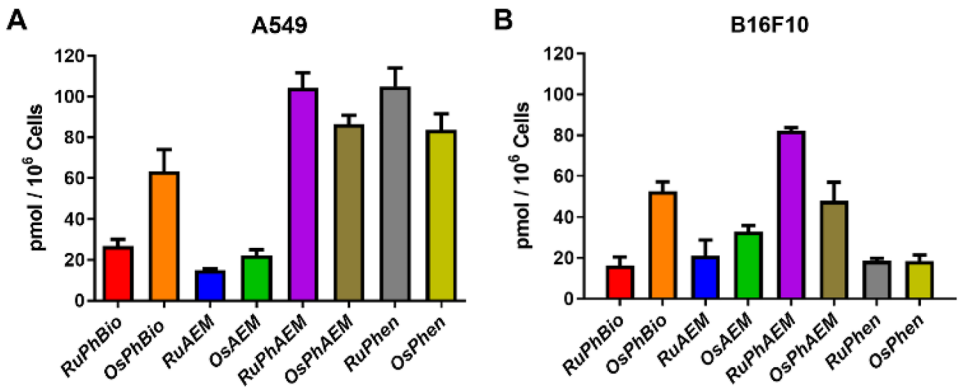

Fig. 4 Intracellular metal contents for RuPhBio, OsPhBio, RuPhen, OsPhen, RuPhAEM, OsPhAEM, RuAEM and OsAEM as determined by ICP-MS on the A549 (**A**) and B16F10 (**B**) cancer cell lines after 24 h exposure at 10 µM

Cellular accumulation

The intracellular metal contents were determined for RuPhBio, OsPhBio, Ruphen and OsPhen by ICP-MS on two cell lines showing either high (A549) expression or low (B16F10) expression of the biotin receptor to verify our design hypothesis (Fig. 4). The expression of the biotin receptor has been extensively studied on various cancer cell lines and reviewed by Kim et al. [24]. An almost identical cellular penetration was found in A549 and B16F10 for both biotin-based complexes and cellular penetration did not correlate to the expression of the biotin receptor, which is in contradiction with our initial hypothesis. The addition of the biotin group did not increase the cellular uptake or the cellular activity when compared to the RuPhen and OsPhen compounds. We can also see that the AEM complexes have low antiproliferative activity, probably as a result of the low intracellular concentrations in both cell lines. The PhAEM complexes, however, and despite having similar or higher intracellular concentrations, have lower antiproliferative activities.

shRNA signatures

We investigated the mechanism(s) of action for the complexes that were the most active in vitro, namely RuPhBio and OsPhBio. We used a multi-variate genetic measurement that is compared to a vast set of known anticancer drugs using supervised and unsupervised machine learning, supervised learning being used to accurately classify anticancer drugs to their respective mechanism. To get proper classification from supervised predictions, the *p*-value threshold was set to 0.05, and the absence of such a significant *p*-value would suggest a novel mechanism. A KNN algorithm, PCA and t-distributed stochastic neighbor embedding (t-SNE) clustering were then applied for the ease of visualization and classification [42–44]. This genetic approach has already been used on promising platinum, Os^{VI} nitrido compounds and for drug reclassification [55–58]. The dendrogram highlights two subgroups of compounds that differ based on their responses on p53 and Chk2 knockdown cell lines (Fig. 5A). The antiproliferative activity of RuPhBio and OsPhBio do not decrease when p53 and Chk2 pathways are down, unlike cisplatin and doxorubicin (Fig. 5A). KNN predictions suggest a "topoisomerase II inhibitors" mechanism for RuPhBio and OsPhBio, however, the non-significant *p* values (> 0.1) indicate an original and/or mixed mechanism of action. This unique mechanism of action is emphasized by the PCA plots showing two distinct sub-groups (Fig. 5B, C). From the t-SNE map, RuPhBio and OsPhBio show spatial proximity with each other but also with mitotic spindle inhibitors, the histone deacetylase (HDAC) and DNA methyltransferase (DNMT) inhibitors, which is different from the KNN predictions, potentially explaining these non-significant *p*-values and validating a multitarget profile.

Conclusions

Six new Ru and Os piano-stool complexes were designed using morpholine and biotin groups to improve the antiproliferative activity of the known [Ru or Os(η^6-*p*-cymene) Cl(1,10-phenanthroline)] complexes. These novel metal complexes demonstrated rather poor cytotoxic activity, the OsPhBio complex reaching an IC_{50} about 77 µM against MCF-7 cell line. We then investigated the potential cellular pathways that may be at play in this activity using a RNAi-based approach, suggesting an original mechanism of action, distinct from the topoisomerase II inhibitors but close to it and mitotic spindle, HDAC and DNMT inhibitors. We showed that the mostly accepted mechanism of action for such Ru and Os compounds (i.e. aquation and reaction with nucleobases and/or proteins) may not have a major role for these biotinyl complexes. A further reactivity study highlighted significant differences toward aquation for metal complexes bearing different sp^2 or sp^3 nitrogen donors. The 1,10-phenanthroline sp^2 ligand tends to give more reactive

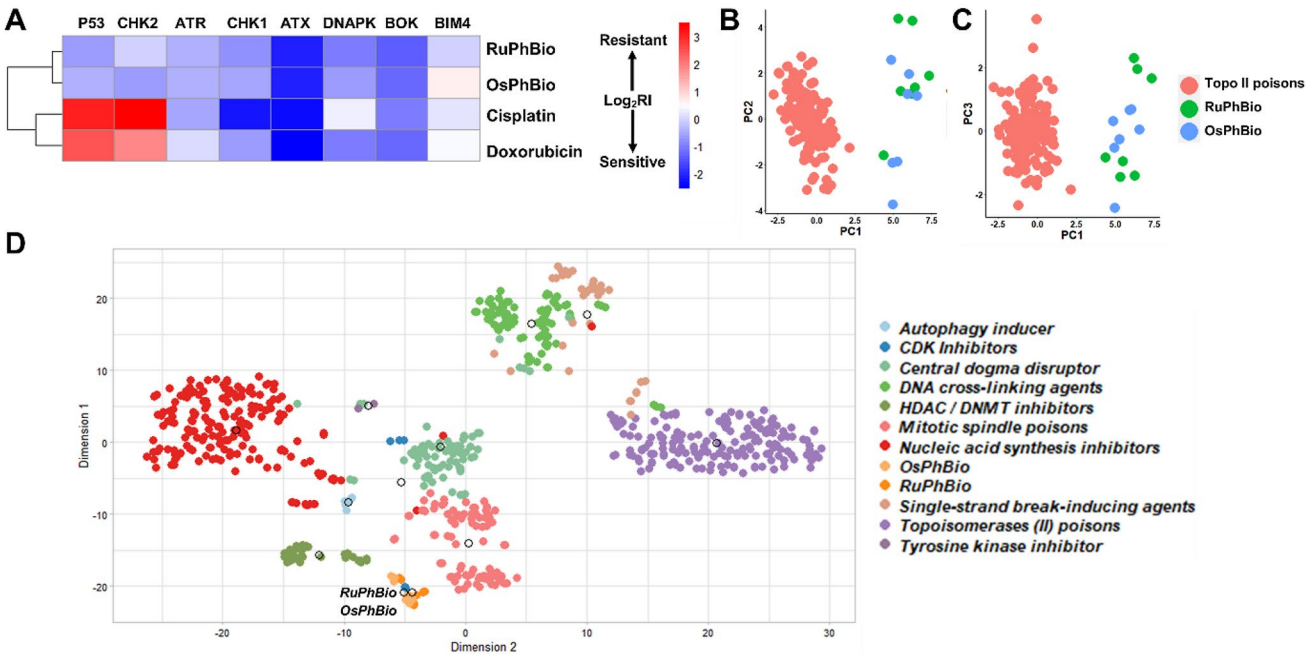

Fig. 5 **A** Heatmap of log_2RI calculated from experimental resistance index determined using eight Eμ-Myc knockdown cell lines. **B**, **C** PCA plots of Log_2RI for topoisomerase II poisons and for compounds RuPhBio and OsPhBio on the eight Eμ-myc knockdown cell lines. **D** 2-D plot generated by t-SNE with the RI obtained for multiple approved antitumor drugs. Centroid points of each area are highlighted by a black circle

complexes in aqueous media, unlike the sp^3 hybridized AEM series chelated with 4-(2-aminoethyl)morpholine that are inert at 37 °C. This trend is mostly related to the presence of the tertiary amine from the morpholino ligand; ethylene diamine complexes having comparable reactivity with water than the sp^2 phen and readily reacts at room temperature. These experimental results are supported by theoretical evidence and DFT-calculated $\Delta G^{\ddagger}$.

Supplementary Information The online version contains supplementary material available at https://doi.org/10.1007/s00775-021-01873-9.

Acknowledgements M.M. thanks Sabrina Cauchies for the ICP-MS experiments.

Author contributions MM and GB conceived and designed the research program. JRP, HI and CJM participated the shRNA experiments. The manuscript was written by MM and GB with contributions from all the authors. MM prepared all figures.

Availability of data and material Crystal structures have been filed in the Cambridge Crystallographic Data Centre (CCDC). Deposit numbers: 2061654 for RuAEM and 2061655 for OsAEM.

Declarations

Conflict of interest The authors declare no competing financial interests.

References

1. Rosenberg B, Van Camp L, Krigas T (1965) Inhibition of cell division in Escherichia coli by electrolysis products from a platinum electrode. Nature 205:698–699. https://doi.org/10.1038/205698a0
2. Galluzzi L, Senovilla L, Vitale I et al (2012) Molecular mechanisms of cisplatin resistance. Oncogene 31:1869–1883. https://doi.org/10.1038/onc.2011.384
3. Florea A-M, Büsselberg D (2011) Cisplatin as an anti-tumor drug: cellular mechanisms of activity, drug resistance and induced side effects. Cancers (Basel) 3:1351–1371. https://doi.org/10.3390/cancers3011351
4. Trondl R, Heffeter P, Kowol CR et al (2014) NKP-1339, the first ruthenium-based anticancer drug on the edge to clinical application. Chem Sci 5:2925–2932. https://doi.org/10.1039/c3sc53243g
5. Leijen S, Burgers SA, Baas P et al (2015) Phase I/II study with ruthenium compound NAMI-A and gemcitabine in patients with non-small cell lung cancer after first line therapy. Invest New Drugs 33:201–214. https://doi.org/10.1007/s10637-014-0179-1
6. Meier-Menches SM, Gerner C, Berger W et al (2018) Structure–activity relationships for ruthenium and osmium anticancer agents—towards clinical development. Chem Soc Rev. https://doi.org/10.1039/C7CS00332C
7. Aird RE, Cummings J, Ritchie AA et al (2002) In vitro and in vivo activity and cross resistance profiles of novel ruthenium(II) organometallic arene complexes in human ovarian cancer. Br J Cancer 86:1652–1657. https://doi.org/10.1038/sj/bjc/6600290
8. Scolaro C, Bergamo A, Brescacin L et al (2005) In vitro and in vivo evaluation of ruthenium(II)–arene PTA complexes. J Med Chem 48:4161–4171. https://doi.org/10.1021/jm050015d
9. Peacock AFA, Habtemariam A, Ferna R et al (2006) Tuning the reactivity of osmium (II) and ruthenium (II) arene complexes under physiological conditions. J Am Chem Soc 128:1739–1748

10. Zhang P, Sadler PJ (2017) Advances in the design of organometallic anticancer complexes. J Organomet Chem 839:5–14. https://doi.org/10.1016/j.jorganchem.2017.03.038
11. Needham RJ, Sanchez-Cano C, Zhang X et al (2017) In-cell activation of organo-osmium(II) anticancer complexes. Angew Chemie Int Ed 56:1017–1020. https://doi.org/10.1002/anie.201610290
12. Flocke LS, Trondl R, Jakupec MA, Keppler BK (2016) Molecular mode of action of NKP-1339—a clinically investigated ruthenium-based drug—involves ER- and ROS-related effects in colon carcinoma cell lines. Invest New Drugs 34:261–268. https://doi.org/10.1007/s10637-016-0337-8
13. Gifford JB, Huang W, Zeleniak AE et al (2016) Expression of GRP78, master regulator of the unfolded protein response, increases chemoresistance in pancreatic ductal adenocarcinoma. Mol Cancer Ther 15:1043–1052. https://doi.org/10.1158/1535-7163.MCT-15-0774
14. Neuditschko B, Legin AA, Baier D et al (2021) Interaction with ribosomal proteins accompanies stress induction of the anticancer metallodrug BOLD-100/KP1339 in the endoplasmic reticulum. Angew Chemie Int Ed 60:5063–5068. https://doi.org/10.1002/anie.202015962
15. Meier SM, Kreutz D, Winter L et al (2017) An organoruthenium anticancer agent shows unexpected target selectivity for plectin. Angew Chemie Int Ed 56:1–6. https://doi.org/10.1002/anie.201702242
16. Dong B, Song X, Kong X et al (2017) A tumor-targeting and lysosome-specific two-photon fluorescent probe for imaging pH changes in living cells. J Mater Chem B 5:988–995. https://doi.org/10.1039/c6tb02957d
17. Andrew CL, Klemm AR, Lloyd JB (1997) Lysosome membrane permeability to amines. Biochim Biophys Acta Biomembr 1330:71–82. https://doi.org/10.1016/S0005-2736(97)00145-4
18. Fu Y, Habtemariam A, Pizarro AM et al (2010) Organometallic osmium arene complexes with potent cancer cell cytotoxicity. J Med Chem 53:8192–8196. https://doi.org/10.1021/jm100560f
19. Piao S, Amaravadi RK (2016) Targeting the lysosome in cancer. Ann N Y Acad Sci 1371:45–54. https://doi.org/10.1111/nyas.12953
20. Fehrenbacher N, Jäättelä M (2005) Lysosomes as targets for cancer therapy. Cancer Res 65:2993–2995. https://doi.org/10.1158/0008-5472.CAN-05-0476
21. Casini A, Gabbiani C, Sorrentino F et al (2008) Emerging protein targets for anticancer metallodrugs: inhibition of thioredoxin reductase and cathepsin B by antitumor ruthenium(II)-arene compounds. J Med Chem 51:6773–6781. https://doi.org/10.1021/jm8006678
22. Mokesch S, Schwarz D, Hejl M et al (2019) Fine-tuning the activation mode of an 1,3-Indandione-based ruthenium(II)-Cymene half-sandwich complex by variation of its leaving group. Molecules 24:1–15. https://doi.org/10.3390/molecules24132373
23. Hao L, Zhong Y-M, Tan C-P, Mao Z-W (2021) Acidity-responsive phosphorescent metal complexes for cancer imaging and theranostic applications. J Organomet Chem. https://doi.org/10.1016/j.jorganchem.2021.121821
24. Ren W, Han J, Uhm S et al (2015) Recent development of biotin conjugation in biological imaging, sensing, and target delivery. Chem Commun 51:10403–10418. https://doi.org/10.1039/C5CC03075G
25. Muhammad N, Sadia N, Zhu C et al (2017) Biotin-tagged platinum(IV) complexes as targeted cytostatic agents against breast cancer cells. Chem Commun 53:9971–9974. https://doi.org/10.1039/c7cc05311h
26. Jin S, Guo Y, Song D et al (2019) Targeting energy metabolism by a platinum(IV) prodrug as an alternative pathway for cancer suppression. Inorg Chem 58:6507–6516. https://doi.org/10.1021/acs.inorgchem.9b00708
27. Babak MV, Plažuk D, Meier SM et al (2015) Half-sandwich ruthenium(II) biotin conjugates as biological vectors to cancer cells. Chemistry 21:5110–5117. https://doi.org/10.1002/chem.201403974
28. Côrte-Real L, Karas B, Brás AR et al (2019) Ruthenium-cyclopentadienyl bipyridine-biotin based compounds: synthesis and biological effect. Inorg Chem 58:9135–9149. https://doi.org/10.1021/acs.inorgchem.9b00735
29. Teixeira RG, Belisario DC, Fontrodona X et al (2021) Unprecedented collateral sensitivity for cisplatin-resistant lung cancer cells presented by new ruthenium organometallic compounds. Inorg Chem Front. https://doi.org/10.1039/d0qi01344g
30. Martin A. Bennett and Anthony K. Smith (1974) Arene ruthenium (II) complexes formed by dehydrogenation of Cyclo-. J Chem Soc Dalt Trans 0:233–241
31. Stahl SWH (1990) A new family of (arene)osmium(0) and -osmium(II) complexes. Organometallics 9:1876–1881
32. Peacock AFA, Habtemariam A, Moggach SA et al (2007) Chloro half-sandwich osmium (II) complexes: influence of chelated N, N-ligands on hydrolysis, guanine binding, and cytotoxicity. Inorg Chem 46:2966–2967. https://doi.org/10.1021/ic062350d
33. Morris RE, Aird RE, Del Socorro MP et al (2001) Inhibition of cancer cell growth by ruthenium(II) arene complexes. J Med Chem 44:3616–3621. https://doi.org/10.1021/jm010051m
34. Higgins B, DeGraff BA, Demas JN (2005) Luminescent transition metal complexes as sensors: structural effects on pH response. Inorg Chem 44:6662–6669. https://doi.org/10.1021/ic050044e
35. Chai J-D, Head-Gordon M (2008) Long-range corrected hybrid density functionals with damped atom-atom dispersion corrections. Phys Chem Chem Phys 10:6615–6620. https://doi.org/10.1039/b810189b
36. Weigend F, Ahlrichs R (2005) Balanced basis sets of split valence, triple zeta valence and quadruple zeta valence quality for H to Rn: design and assessment of accuracy w. Phys Chem Chem Phys 7:3297–3305
37. Weigend F (2006) Accurate Coulomb-fitting basis sets for H to Rn. Phys Chem Chem Phys 8:1057–1065. https://doi.org/10.1039/b515623h
38. Van LE, Baerends EJ, Snijders JG (1993) Relativistic regular two-component Hamiltonians. J Chem Phys 99:4597. https://doi.org/10.1063/1.466059
39. Glendening ED, Badenhoop JK, Reed AE et al (2013) NBO 6.0. Theor Chem Institute, Univ Wisconsin, Madison
40. Klose MHM, Hejl M, Heffeter P et al (2017) Post-digestion stabilization of osmium enables quantification by ICP-MS in cell culture and tissue. Analyst 142:2327–2332. https://doi.org/10.1039/c7an00350a
41. Berger G, Grauwet K, Zhang H et al (2018) Anticancer activity of osmium(VI) nitrido complexes in patient-derived glioblastoma initiating cells and in vivo mouse models. Cancer Lett 416:138–148. https://doi.org/10.1016/j.canlet.2017.11.041
42. Jiang H, Pritchard JR, Williams RT et al (2010) A mammalian functional-genetic approach to characterizing cancer therapeutics. Nat Chem Biol 7:1–9. https://doi.org/10.1038/nchembio.503
43. Pritchard JR, Bruno PM, Hemann MT, Lauffenburger DA (2013) Predicting cancer drug mechanisms of action using molecular network signatures. Mol Biosyst 9:1604–1619. https://doi.org/10.1039/c2mb25459j
44. Pritchard JR, Bruno PM, Gilberta LA et al (2013) Defining principles of combination drug mechanisms of action. PNAS. https://doi.org/10.1073/pnas.1210419110
45. Landázuri N, Le Doux JM (2006) Complexation with chondroitin sulfate C and polybrene rapidly purifies retrovirus from inhibitors

of transduction and substantially enhances gene transfer. Biotechnol Bioeng 93:146–158. https://doi.org/10.1002/bit.20697
46. Bevernaegie R, Marcélis L, Laramée-Milette B et al (2018) Trifluoromethyl-substituted iridium(III) complexes: from photophysics to photooxidation of a biological target. Inorg Chem 57:1356–1367. https://doi.org/10.1021/acs.inorgchem.7b02778
47. Wang D, Lippard SJ (2005) Cellular processing of platinum anticancer drugs. Nat Rev Drug Discov 4:307–320. https://doi.org/10.1038/nrd1691
48. Marloye M, Berger G, Gelbcke M, Dufrasne F (2016) A survey of the mechanisms of action of anticancer transition metal complexes. Future Med Chem. https://doi.org/10.4155/fmc-2016-0153
49. Betanzos-lara S, Novakova O, Deeth RJ et al (2012) Bipyrimidine ruthenium (II) arene complexes: structure, reactivity and cytotoxicity. J Biol Inorg Chem 17:1033–1051. https://doi.org/10.1007/s00775-012-0917-9
50. Wang F, Chen H, Parsons S et al (2003) Kinetics of aquation and anation of ruthenium(II) arene anticancer complexes, acidity and X-ray structures of aqua adducts. Chem A Eur J 9:5810–5820. https://doi.org/10.1002/chem.200304724
51. Popp J, Hanf S, Hey-Hawkins E (2019) Facile arene ligand exchange in p-cymene ruthenium(II) complexes of tertiary P-chiral ferrocenyl phosphines. ACS Omega 4:22540–22548. https://doi.org/10.1021/acsomega.9b03251
52. Sullivan MP, Nieuwoudt MK, Bowmaker GA et al (2018) Unexpected arene ligand exchange results in the oxidation of an organoruthenium anticancer agent: the first X-ray structure of a protein–Ru(carbene) adduct. Chem Commun. https://doi.org/10.1039/C8CC02433B
53. Hubig SM, Lindeman SV, Kochi JK (2000) Charge-transfer bonding in metal-arene coordination. Coord Chem Rev 200–202:831–873. https://doi.org/10.1016/S0010-8545(00)00322-2
54. Adeniyi AA, Ajibade PA (2013) Insights into the intramolecular properties of η 6-arene-Ru-based anticancer complexes using quantum calculations. J Chem. https://doi.org/10.1155/2013/892052
55. Bruno PM, Liu Y, Park GY et al (2017) A subset of platinum-containing chemotherapeutic agents kills cells by inducing ribosome biogenesis stress. Nat Med 23:461–471. https://doi.org/10.1038/nm.4291
56. Zheng YR, Suntharalingam K, Bruno PM et al (2016) Mechanistic studies of the anticancer activity of an octahedral hexanuclear Pt(II) cage. Inorganica Chim Acta 452:125–129. https://doi.org/10.1016/j.ica.2016.03.021
57. Suntharalingam K, Johnstone TC, Bruno PM et al (2013) Bidentate ligands on osmium(VI) nitrido complexes control intracellular targeting and cell death pathways. J Am Chem Soc 135:14060–14063. https://doi.org/10.1021/ja4075375
58. Bruno PM, Lu M, Dennis KA et al (2020) The primary mechanism of cytotoxicity of the chemotherapeutic agent CX-5461 is topoisomerase II poisoning. Proc Natl Acad Sci USA 117:4053–4060. https://doi.org/10.1073/pnas.1921649117

Authors and Affiliations

Mickaël Marloye[1] · Haider Inam[2] · Connor J. Moore[2] · Vinciane Debaille[3] · Justin R. Pritchard[2] · Michel Gelbcke[1] · Franck Meyer[1] · François Dufrasne[1] · Gilles Berger[1,4]

[1] Microbiology, Bioorganic and Macromolecular Chemistry, Faculté de Pharmacie, Université Libre de Bruxelles (ULB), 1050 Brussels, Belgium

[2] Department of Biomedical Engineering, Pennsylvania State University, University Park, PA, USA

[3] Laboratoire G-Time, Université Libre de Bruxelles, 1050 Brussels, Belgium

[4] Harvey Cushing Neuro-Oncology Laboratories, Department of Neurosurgery, Brigham and Women's Hospital, Harvard Medical School, Boston, MA, USA